Manuscript title

Tracking Discrete Off-resonance markers with Three Spokes (trackDOTS) for compensation of head motion and B_0 perturbations: accuracy and performance in anatomical imaging

Authors

João Jorge,[1] Frédéric Gretsch,[1] Daniel Gallichan,[2] José P. Marques[3,*]

Affiliations

[1] Laboratory for Functional and Metabolic Imaging, École Polytechnique Fédérale de Lausanne, Lausanne, Switzerland

[2] Biomedical Imaging Research Center, École Polytechnique Fédérale de Lausanne, Lausanne, Switzerland

[3] Donders Institute, Radboud University, Nijmegen, the Netherlands

Word count: 6306

Running title: TrackDOTS – a new approach for head motion and field monitoring

Keywords: retrospective motion correction, B_0 field monitoring, trackDOTS, navigators

***Corresponding author:**

José P. Marques

Kapittelweg 29

6525 EN Nijmegen

the Netherlands

E-mail: j.marques@donders.ru.nl ‖ Telephone/fax: +31 024-3668491

Abstract

(word count: 201)

Purpose: To develop a novel approach for head motion and B_0 field monitoring based on tracking Discrete Off-resonance markers with Three Spokes (trackDOTS).

Methods: Small markers filled with acetic acid were built and attached to a head cap. Marker positions and phase were tracked with fast MR navigators (DotNavs) comprising three off-resonance, double-echo orthogonal 1D-projections. Individual marker signals were extracted using optimized coil combinations, and used to estimate head motion and field perturbations. To evaluate the approach, DotNavs were integrated in sub-millimeter MP2RAGE and long-TE GRE sequences at 7T, and tested on six healthy volunteers.

Results: DotNav-based motion estimates differed by less than 0.11±0.09mm and 0.19±0.17° from reference estimates obtained with an existing navigator approach (FatNavs). Retrospective motion correction brought clear improvements to MP2RAGE image quality, even in cases with sub-millimeter involuntary motion. DotNav-based field estimates could track deep breathing-induced oscillations, and in cases with small head motion, field correction visibly improved GRE data quality. Conversely, field estimates were less robust when strong motion was present.

Conclusion: The trackDOTS approach is suitable for head motion tracking and correction, with significant benefits for high-spatial resolution MRI. With small head motion, DotNav-based field estimates also allow correcting for deep-breathing artifacts in T_2^*-weighted acquisitions.

Introduction

Due to their inherently low signal-to-noise ratio (SNR), together with the characteristic timescales of nuclear magnetic resonance relaxation in vivo, magnetic resonance imaging (MRI) and spectroscopy acquisitions of the brain typically last for several minutes. During this time, a patient will have necessarily gone through several cardiac and respiratory cycles, and even a cooperative subject can be expected to move by up to a few millimeters (1), altogether leading to image quality degradation. Artifacts due to head motion include ringing, blurring and ghosting (2), which depend on the amplitude and timing of occurrence of movements during the acquisition. The respiratory cycle, in addition, involves chest motion together with changes in air volume inside the lungs, which change the local magnetic susceptibility, affecting the B_0 field distribution in nearby regions such as the head (3). Sequences requiring longer echo times (TE) such as T_2^*-weighted imaging, susceptibility-weighted imaging (4) and quantitative susceptibility mapping (5) are the most affected by these contributions, with artifacts such as ghosting, signal loss, ringing, blurring and intensity modulations (6).

For less-cooperative subject groups, such as very young or elderly patients, motion-related artifacts can often be strong enough to hinder identification of important features and render the images unusable for clinical diagnosis, potentially requiring repeated exams. Moreover, the development of ultra-high field systems, offering significant gains in MR signal strength, has allowed for the pursuit of sub-millimeter spatial resolution. For such voxel sizes, even very small involuntary movements can produce appreciable artifacts, preventing a full exploitation of the potential gains of ultra-high field imaging. Likewise, because magnetic susceptibility effects scale with B_0, respiration-induced field fluctuations also tend to be accentuated at higher fields, curbing the increased sensitivity for biologically-relevant susceptibility differences. Overall, it has become clear that tracking and accounting for motion and breathing-related effects is highly important to obtain robust, high-quality MRI data, and particularly to make the most of the sensitivity gains available at higher fields (2,3,7-9).

Various methods have been proposed to monitor head motion during MR scans, including the use of external cameras (2,10-12), image (13-15) or free induction decay-based navigators (16,17), and MR field probes (18,19). Motion tracking information can be used to correct for its effects either in a so-called prospective manner, where the acquisition is adjusted in real-time to compensate for changes in head position and orientation (10,11), or retrospectively, during image

reconstruction (7,20). While some of the most impressive results in prospective motion correction to date, in terms of precision and latency, have been obtained using external camera setups (2,10), the integration of optic cameras with MR systems involves additional hardware, optical markers and calibration procedures, and requires a clear line-of-sight between the camera and the head, which is in some cases not feasible. Furthermore, optical methods are not suitable for monitoring magnetic field fluctuations. As an alternative, MR field monitoring probes can be made capable of tracking both head motion (18) and field fluctuations (19), but these approaches also typically require specialized external hardware to be integrated with the MR scanner (21).

As an alternative to optical and field probe-based methods, so-called MR-based approaches have been proposed which rely mainly on MR signals from the head itself, measured across time with specific acquisition modules (navigators) integrated in the main MR sequence. Apart from modifications in the host sequence, most of these methods require no additional hardware or synchronization between devices. On the other hand, it can often be challenging to integrate navigators into the host sequences without disturbing the MR signal of interest or lengthening the total host acquisition time (TA), typically requiring compromises between accuracy, temporal resolution, and the TA of the navigators. Recently, the use of 3D images of the fat tissues in the head (FatNavs) has been explored for motion tracking (20,22). The sparsity of fat in the head was found to permit a high degree of k-space undersampling without appreciable losses in sensitivity, allowing for robust motion tracking with navigators acquired in as little as 144 ms (23). This solution is particularly well suited for water imaging sequences that already include regular dead-time periods, such as T_1-weighted sequences at 7 T (20). Nevertheless, the inclusion of a single navigator per inversion cycle restricts its sampling period to at least a few seconds, and additional inclusions will likely require compromises in the total TA or other host sequence parameters. This can be even more problematic for sequences such as T_2^*-weighted GRE, where there is typically no dead-time available and the inclusion of navigators will lead to an increase in total scan time. Overall, the challenge of motion and field monitoring remains an open problem in MR, with different approaches carrying different advantages and compromises.

In this work, we explore a novel approach for simultaneous head motion and B_0 field monitoring based on tracking Discrete Off-resonance markers with Three Spokes (trackDOTS). This approach relies on fast MR navigators ($\leq$ 45 ms per measurement) and requires no additional recording hardware, besides the use of a receive coil array for acquisition (preferably with a large

number of channels). The approach relies on measuring MR signals from a set of small spherical markers filled with a liquid rich in hydrogen nuclei with a resonance frequency significantly different from that of water and fat – but still within the typical band accepted by the MR system. These markers are distributed and attached to the subject's head, and monitored with navigators hereafter termed "DotNavs". Each DotNav excites the markers with frequency-selective pulses, to acquire three orthogonal projections of the full field of view. The markers captured together in the projections are then separately identified based on prior knowledge of the receive coil array sensitivities, and their positions uniquely determined. The field perturbations in each marker are also measured by acquiring two echoes per projection, thereby allowing for concurrent field monitoring. This approach was implemented at 7 T and tested on a group of healthy subjects. DotNav-based motion tracking and retrospective image correction was investigated on a T_1-weighted anatomical sequence, with and without induced subject motion, and its performance was compared to that of FatNav-based correction. The impact of field monitoring and correction was investigated on a T_2^*-weighted acquisition, during natural as well as deep breathing.

Methods

All MRI acquisitions were performed on a Magnetom 7 T head scanner (Siemens Healthcare, Erlangen, Germany) equipped with AC84 gradients and a birdcage transmit/32-channel receive RF coil array (Nova Medical, Wilmington MA, USA). The estimation and correction of motion and field perturbations were performed retrospectively, using custom routines developed in Matlab (MathWorks, Natick MA, USA).

Marker design

In this work, the trackDOTS markers were implemented as 3D-milled hollow spheres made of polyether ether ketone (PEEK), filled with an acetic acid solution. The spheres were designed with an inner diameter of 8 mm and outer diameter of 12 mm (Fig. 1a), found to yield an acceptable compromise between marker SNR (volume of liquid) and subject comfort. The spherical shape ensured independence of the marker signal and projections from its current orientation, as well as to improve static field homogeneity inside the marker.

Acetic acid contains three protons resonating at 2 ppm (methyl group), and one proton at 11.6 ppm (acid group, Fig. 1b). The resonance signal from the acid proton was chosen as the target of

interest, its peak lying at a reasonable distance from the water (4.7 ppm) and main fat peak (1.2 ppm). The liquid was doped with MnCl at a concentration of 0.25 g/l, and the final markers exhibited apparent T_1 and T_2^* constants of approximately 26 ms and 4.6 ms, respectively. A total of 12 markers were assembled and tightly fixed to an EEG-like head cap (EasyCap, Herrsching, Germany), in distributed positions over the head (Fig. 1c,d).

Navigators and host sequences

The navigators used to monitor the trackDOTS markers (DotNavs) consisted of three marker-selective, 1D orthogonal projections of the head field-of-view (FOV) (Fig. 2a). Marker-selective excitation was attained using a sinc pulse with a frequency offset of +2000 Hz relative to the reference water signal (i.e. at 11.6 ppm), with 30° flip angle, 3 ms pulse duration, BW = 667 Hz. After excitation, a frequency-encoded readout with two echoes was played along the X, Y or Z direction (TE_1/TE_2 = 3.1/6.1 ms, 781 Hz/Px bandwidth). In between the excitation and the first readout, pre-phaser gradients were applied in the other two spatial directions, designed to dephase the signal with a spatial periodicity of 16 mm (twice the marker diameter). This was intended to cancel out spurious signal contributions from head regions larger than the markers, arising due to B_0 inhomogeneities in the head and imperfect frequency profile of the RF pulse, while preserving the marker signals (24). Spoiler gradients were applied after the second readout. Each projection was set with a TR of 15 ms, resulting in a TA of 45 ms per DotNav measurement.

The performance of trackDOTS-based motion tracking and correction for T_1-weighted imaging was investigated using a flow-compensated 3D MP2RAGE host sequence (25), with 0.6 mm isotropic spatial resolution, 192×192×154 mm FOV, $TE/TI_1/TI_2/TR$ = 4.94/800/2700/6000 ms, α_1/α_2 = 7°/5°, 3× GRAPPA acceleration in the first phase-encoding direction and 6/8 partial Fourier undersampling in both phase-encoding directions, and a total TA of approximately 10 min. Within each k-space plane acquisition, the dead-time available between the second GRE readout and the next inversion pulse was long enough to allow including both a DotNav and a FatNav acquisition (Fig. 2b). As in previous work (20), the FatNavs consisted of highly-undersampled 3D GRE images of the fat signal, and were acquired with 2 mm isotropic resolution, TE/TR = 1.4/3.0 ms, 4×4 GRAPPA and 6/8 partial Fourier undersampling in both phase-encoding directions, resulting in a TA of 1.15 s.

B_0 field monitoring was first tested by integrating DotNavs in a fast double-echo 3D GRE sequence, with 5 mm isotropic resolution, 220×180×120 mm FOV, TE_1/TE_2 = 1.65/3.44 ms, 3× GRAPPA acceleration in one phase-encoding direction and 6/8 partial Fourier in both phase-encoding directions, for a total TA of 1.8 s. This allowed for concurrent GRE-based and trackDOTS-based field measurements with a temporal resolution of 1.8 s, with the former serving as "gold standard" for testing. The impact of field monitoring and correction was investigated on a flow-compensated 3D GRE sequence with 0.5×0.5×1 mm resolution, 192×192×36 mm FOV, α = 7º and 6/8 partial Fourier undersampling in both phase-encoding directions. A DotNav measurement was inserted after every (coronal) k-space plane acquisition, yielding a temporal resolution of 1.4 s. A TE of 27 ms was adopted, which confers a strong T_2^*-weighting and offers improved phase contrast for certain applications (26), while also being reasonably sensitive to B_0 perturbations. The total host TA was approximately 6.6 min.

Marker identification

Each DotNav projection is expected to show twelve peaks distributed within the FOV (one per marker). In order to uniquely identify which marker each peak belongs to, marker-specific RF coil combinations were first determined, optimized to yield maximal sensitivity to a single marker while minimizing sensitivity to the remaining markers and other signal contaminations. To determine the optimal coil combinations, two fast 3D GRE acquisitions were included in the protocol before the main sequences: (i) a marker-selective image (excitation frequency offset = 2000 Hz, 1.75 mm isotropic resolution, 8× GRAPPA acceleration, TA = 20 s), and (ii) a water image (3.5×3.5×1.75 mm resolution, 4× GRAPPA acceleration, TA = 8.3 s). The marker-selective image was used to identify the initial position of each marker, following an automatic procedure that comprised: (1) locating the voxel of maximum intensity in the image, (2) associating this position to a marker index, (3) setting the voxel and its neighbors within a 10-voxel radius to zero intensity, and then repeating steps 1–3 until every marker is identified.

Having obtained the initial marker positions, the water image was then used to determine the marker-specific coil combinations. First, a brain mask was obtained by simple thresholding of the water magnitude image. For each marker m, two regions-of-interest (ROIs) were then defined: a "preservation" ROI, R_p^m, comprising a sphere of radius ρ centered on the marker position, and an "exclusion" ROI, R_e^m, comprising the brain mask (excluding R_p^m) and the preservation ROIs of

the other markers. An optimal linear coil combination C^m was then sought to minimize the signal magnitude within $R_e{}^m$ while keeping the average intensity in $R_p{}^m$ close to a fixed non-zero value. This was described by the following cost function:

$$E(C^m) = \frac{1}{N_p^m} \sum_{i \in R_p^m} (|A_i C^m| - a)^2 + \frac{\lambda}{N_e^m} \sum_{i \in R_e^m} |A_i C^m|^2 \quad [1]$$

where A_i is a complex $1 \times N_c$ array containing the signal at voxel i given by each coil, N_c is the number of available coils, C^m is a complex $N_c \times 1$ array containing the linear coil combination coefficients, $N_p{}^m$ and $N_e{}^m$ are the number of voxels within the preservation and exclusion ROIs, and a and λ are positive constants. Based on initial tests, the $R_p{}^m$ radius ρ was set to 21 mm and the cost parameter λ to 10^6 – both representing a compromise between specificity for the marker signal and flexibility to future displacements from its original position.

Motion estimation and correction

Having determined the optimal coil combination for each marker, the combination coefficients were then applied to the multi-coil DotNav projection data acquired within the host protocol, resulting in 12 marker-specific X, Y and Z-projections per timepoint (i.e. per MP2RAGE k-space plane acquisition). Only the first echo was used for this part (the second-echo projections were typically of lower SNR). For each marker-specific projection, the signal maximum was identified within a 2ρ window centered at the initial reference position, and the signal was then integrated over an 8 mm window centered at the maximum, to find its center of mass. The center of mass was taken as the marker position along that projection. Head motion was then estimated by finding the rigid body transformation M^t that minimizes the distance between the set of marker positions at each timepoint t, P^t, and a reference set P^0 (here chosen as the set from the first DotNav measurement). This formulation allowed the inclusion of marker- and coordinate-specific weights for each marker coordinate, important for down-playing contributions from poor-quality projections to the global motion estimate. This was implemented with a robust least-squares optimization approach, based on the following cost function:

$$E(M^t) = \sum_{\substack{m \in Markers \\ i = x,y,z}} w_{m,i} \left(p^t_{m,i} - M^t_i \begin{bmatrix} p^0_{m,x} \\ p^0_{m,y} \\ p^0_{m,z} \\ 1 \end{bmatrix} \right)^2 \quad [2]$$

where $p^t_{m,i}$ is the estimated position of marker m at time t and coordinate i, M_i^t is the i^{th} row of the 3×4 matrix M^t, and $w_{m,i}$ is a non-negative scalar weight for the contribution of coordinate i from marker m. The cost function E was minimized through a simple gradient descent approach. The weights were determined through repeated minimizations of E, being iteratively updated as a function of the residual error $E_{m,i}$ of each marker coordinate relative to the transformed reference (the larger the error, the smaller the new weight). A total of 5 iterations was found to produce stable weights for the tested datasets.

For comparison purposes, head motion estimation was also performed using the concurrently acquired FatNavs, employing the *realign* tool from SPM (Statistical Parametric Mapping, v.8), as described in (20). Finally, the host MP2RAGE data was corrected for motion effects using either the DotNav- or FatNav-derived motion information: the estimated translations and rotations were applied to the corresponding k-space planes (20), with translations corresponding to simple phase ramps in k-space, and rotations requiring 3D regridding, which was performed using the non-uniform fast Fourier transform algorithm (27) provided by Jeffrey Fessler's reconstruction toolbox (http://web.eecs.umich.edu/~fessler/code/). All corrections were performed separately for each GRE readout and channel, prior to calculating the final MP2RAGE image.

To further evaluate the compromise between accuracy and speed achieved with DotNavs, the originally-acquired FatNavs were systematically subsampled by cropping k-space to achieve voxel sizes of 4 / 6 / 8 / 10 mm, corresponding to acquisition times of 288 / 128 / 72 / 46 ms, respectively. These "accelerated" navigators were then also used for head motion estimation, for comparison with the original FatNavs as well as the DotNavs, for all subject acquisitions with and without induced motion.

Field monitoring and correction

Similar to the MP2RAGE acquisition, the DotNav projections acquired during the fast double-echo GRE and the long-TE GRE sequences were initially combined across coil channels to yield 12 marker-specific X, Y and Z-projections per timepoint. The marker positions and motion

parameters were also estimated as previously described. Additionally, to detect B_0 fluctuations, a second set of marker projections was obtained from the second echo of the DotNavs. For each marker projection, the complex signal at the marker position from the second echo was multiplied by the complex conjugate of that of the first echo, and re-referenced to the first timepoint by another multiplication. The phase of the resulting value was then extracted and scaled by $2\pi\Delta TE$, to yield a measure of field shifts, ΔB, with respect to the first measurement. For the data tested in this work, phase unwrapping was not found to be necessary. Having measured a set of marker positions and field shifts for each timepoint, the underlying spatial distribution was modeled as a linear combination of an offset (0^{th} order) term ΔB^0 and 1^{st} order terms $G_x x$, $G_y y$, $G_z z$. These parameters were estimated with a second robust linear regression approach, analogous to that used for motion estimation.

After B_0 field estimation, for the fast double-echo GRE runs, the DotNav-based field estimates were compared to the concurrent reference estimates given by the double-echo images, in terms of the average absolute difference between the two estimates. The temporal correlation of these field timecourses with the head motion timecourses was also evaluated. For the long-TE GRE acquisitions, after motion and field estimation, both effects were jointly corrected for, for each GRE k-space plane. Using the same k-space framework as previously described for the MP2RAGE, the 0^{th} order term of ΔB was accounted for in phase correction together with head translations, and the 1^{st} order terms corresponded to k-space shifts, implemented with a non-uniform fast Fourier transform together with head rotations (28).

Human acquisitions

After implementation, the trackDOTS approach was tested on six healthy human volunteers (4 male, 2 female, aged 27±3 years old), who provided informed consent prior to the scan, under approval from the institutional review board of the local ethics committee. Each subject was fitted with the trackDOTS cap and underwent four anatomical acquisitions: A - MP2RAGE acquisition while lying still in the scanner, B - MP2RAGE with externally-induced motion, C - GRE acquisition while lying still and breathing normally, and D - GRE during slow, deep breathing. In two of the subjects, the accuracy of trackDOTS-based field monitoring was also tested with the fast double-echo GRE host protocol (E), acquired repeatedly in two sessions of 5 min (170 volumes per session), during deep and normal breathing, respectively. Due to time

constraints, one of the six subjects did not undergo acquisitions C and D. The induced motion procedure (acquisition B) was conducted with an air cushion placed under the subject's head, as proposed in previous work (23). The cushion was slowly deflated during the first 4 min of acquisition, and then reflated during a similar period, inducing a slow head drift mainly in the sagittal plane. For acquisitions C–E, the subject's respiratory amplitude was also recorded using a pneumatic belt (50 Hz sampling rate) from the physiological monitoring unit of the scanner. The reference water and marker-selective images were also acquired before each of the anatomical sequences, resulting in a total scan time of approximately 43 min per subject.

Results

TrackDOTS implementation

In its current proof-of-concept design, the head cap with attached markers was generally well-tolerated by the participating subjects. Most subjects did report a moderate discomfort increasing after the first 30 min of acquisition, mainly due to two of the markers which lay under the head close to more protuberant skull regions. Due to the susceptibility-related B_0 perturbations created by the human head (29), affecting regions both within and around the head, the resonance frequencies of the markers were observed to vary between approximately +1800 and +2200 Hz relative to the water peak frequency, depending on their position.

In order to evaluate the impact of different methodological steps on the ability to measure individual marker signals, a "peak quality" measure Q_p for each projection was defined as $Q_p = (\overline{S_m} - \overline{S_b})/\overline{S_m}$, where $\overline{S_m}$ is the average signal in an 8 mm window centered on the marker position, and $\overline{S_b}$ is the average signal in two 8 mm windows directly to each side of the marker window (considered background). For an ideal peak without noise or signal contaminations, Q_p will equal 1; in real measurements it will be lower. Overall, the optimization approach adopted to determine marker-specific coil combinations proved effective in isolating each marker (Fig. 3a), and across markers and subjects, the approach yielded a 30±6% increase in peak quality relative to a simpler method where each projection is given solely by the nearest coil. The use of pre-phaser gradients prior to the readout was also found to be highly beneficial to suppress spurious signal contributions from the head (Fig. 3b). In a separate test performed on a single subject, the use of pre-phasers was observed to yield a 93±27% increase in peak quality, across markers,

when compared to non-phased projections. Overall, for the data collected in this study, the proposed methodology yielded appreciably good-quality projections for most markers (Fig. 4), with an average peak quality of 0.86±0.01 across subjects and markers.

The PEEK enclosing proved generally effective in preventing CH_3COOH evaporation. Over a period of approximately two years, three of the twelve markers showed signs of evaporation (manifesting as a reduction in Q_p and the presence of an air bubble slightly altering the shape of the projection peaks), and were thereby replaced by new markers.

Motion estimation and correction

According to both DotNav and FatNav estimations, the externally-induced motion led to slow, drift-like head translations ranging up to approximately 0.44 / 1.79 / 1.11 mm in the X/Y/Z-direction (i.e. left-to-right / posterior-to-anterior / feet-to-head), and rotations up to 1.77 / 0.52 / 0.73° around the X/Y/Z-axis (i.e. pitch / roll / yaw) (Fig. 5, left). Without induced motion, the movement parameters were more moderate, with translations up to approximately 0.32 / 0.31 / 0.39 mm and rotations up to 0.57 / 0.43 / 0.47° (Fig. 5, right).

In general, a good agreement was found between DotNav and FatNav estimates (Fig. 6), with average absolute deviations between the two of 0.04±0.03 / 0.10±0.09 / 0.08±0.06 mm for translations, and 0.21±0.19 / 0.09±0.08 / 0.14±0.13° for rotations, across subjects and both run types. For both translations and rotations, the DotNavs exhibited a small but consistent trend for underestimation relative to FatNavs, which could be observed in global (Fig. 6) as well as in individual subject estimates. For the acquisitions performed with induced motion, the correction of motion effects during the MP2RAGE image reconstruction led to visible improvements in image quality, with reduced ghosting and ringing effects, and sharper edges evident in structures such as the cortical surface, ventricles and vessels (Fig. 7 A). This was generally observed in both FatNav and DotNav-informed reconstructions. For three of the subjects, both corrections were of comparable quality, whereas in the other three the FatNav approach yielded slightly superior results – particularly in cases of underestimation from the DotNavs relative to the FatNavs. In the acquisitions without induced motion, all subjects remained considerably still, and the images were found to be of good quality overall, even without correction. Nevertheless, in two of the six subjects, visible improvements could still be found with both DotNav and FatNav corrections

(Fig. 7 B,C), even with translations below 0.27 mm and rotations below 0.37°. In the other four subjects, neither type of correction produced discernible changes in the images.

Motion estimation using the accelerated FatNavs created post-acquisition showed that increasing acceleration led to increasing deviations relative to the originally-acquired FatNavs. The DotNav estimates tended to outperform those of FatNavs accelerated by 5× to a TA of 46 ms, and were roughly at the level of 4×-accelerated, 72 ms FatNavs (Fig. 8).

Field monitoring and correction

Based on DotNav estimates, B_0 field perturbations ranged up to 5 Hz (offset term) and 74 / 91 / 174 Hz/m ($G_x/G_y/G_z$) during normal breathing, and higher up to 7 Hz and 89 / 126 / 216 Hz/m during deep breathing, on average across subjects. In the two subjects tested with the double-echo GRE protocol, DotNav estimates exhibited average absolute deviations of 0.6 Hz and 7.4 / 7.3 / 17.2 Hz/m during normal breathing, and 0.9 Hz and 6.7 / 15.1 / 18.4 Hz/m during deep breathing, relative to reference field estimates from the double-echo GRE images (Fig. 9). Across the two subjects and run types, the DotNav field estimates were consistently more correlated to the head motion parameters than the double-echo GRE estimates, and the deviations between the two tended to be larger in the cases where correlation with motion was higher as well. In particular, comparing the cases of lowest and highest correlation with motion, increases of 5.0× (offset term) and 2.2 / 19.0 / 4.9× ($G_x/G_y/G_z$) in absolute deviation were observed. Overall, in deep breathing runs, the DotNav measurements proved sensitive enough to track oscillations coupled to the breathing cycle (Fig. 9) in all subjects. These oscillations were generally most prominent in the offset and G_z terms.

The DotNav-informed correction of field perturbations during the high-resolution GRE image reconstruction yielded mixed results for the acquired dataset. In the deep breathing run, two subjects performed the task with little head motion, and the corresponding field-corrected images exhibited clear improvements, including ghosting reduction, increases in grey-matter to white-matter contrast and mitigation of localized signal loss (Fig. 10, Supporting Fig. S1 A). However, this was achieved by using only the field offset term for correction – the estimated 1st order terms tended to produce worse-quality images, and had to be excluded. Furthermore, in the other three subjects, the breathing task was coupled to larger head motion, and the corrected images, apart from minor improvements, remained of poor quality (Supporting Fig. S1 B). Importantly, in these

subjects, field correction (with the offset term only) yielded improvements only when the field timecourse was first filtered by regressing out the motion timecourses (Supporting Fig. S1 B). Finally, for the normal-breathing run, the GRE images were, as expected, significantly less corrupted by artifacts (Supporting Fig. S2). Motion correction had a negligible effect for two of the subjects; for the remaining three, visible improvements were still obtained. The joint correction of motion and field effects did not, however, produce conclusive further improvements in image quality.

Discussion

In this work, a novel approach was developed for simultaneous tracking of head motion and B_0 perturbations during MRI acquisition, using a set of off-resonance markers attached to the head and measured with fast navigators based on three orthogonal projections. The approach was implemented at 7 T and tested on six healthy volunteers, and its performance was investigated for a T_1-weighted and a T_2^*-weighted MRI sequence, at high spatial resolution.

TrackDOTS-based motion correction

In this study, to evaluate the accuracy of trackDOTS-based motion estimates, FatNavs were included in the same MP2RAGE host sequence and served as a reference or "gold standard" for comparison. FatNav-based motion correction has been previously validated and optimized to a considerable extent, particularly for the type of slow drift-like motion explored in this work (23). Consistent with this, for all acquired MP2RAGE data, FatNav-informed reconstructions resulted in practically artifact-free images, clearly superior in quality to non-corrected reconstructions. For the same data, DotNav-derived motion estimates showed absolute deviations to FatNav estimates in the order of 0.1 mm (well below the image spatial resolution of 0.6 mm) and 0.2°. DotNav-informed reconstructions consistently showed superior image quality to non-corrected images, and were in some cases indiscernible from the FatNav-based approach (Fig. 7). Naturally, as expected, the impact of motion correction was considerably more evident in images acquired with externally-induced motion. Nevertheless, the motion patterns created in this manner were of fairly small amplitude (below 2 mm / 2º) considering those often observed in less compliant subjects, and similar in shape to common head drift patterns. Furthermore, in two of the six acquisitions without induced motion, both navigators still yielded visible improvements even in

the presence of small involuntary motion (Fig. 7 B,C), evincing the high sensitivity of both methods, as well as the importance of motion artifact correction for high-resolution imaging.

For the MP2RAGE data collected in this work, DotNav estimates exhibited a small but consistent bias for motion underestimation compared to FatNav estimates, both in translations and rotations (Fig. 6). A probable reason for this is the presence of dragging effects between certain markers, the head and the coil, impeding the markers from following the head as rigidly as desired. In the current setup, the markers were tightly attached to the head cap, but the cap itself was flexible, allowing for moderate stretches. This non-rigidity problem, which is not exclusive to this approach (2), can potentially be mitigated in future implementations with more rigid attachment (18,30). A second possibility is a deleterious influence of signal contaminations on the localization of marker projection peaks. More specifically, the projections of bulk contributions from the head are expected to change with rotation, but likely not in a consistent way with the marker positions, leading to biases. Such a confound could possibly be reduced by increasing marker SNR, for example with larger makers, or by choosing a different off-resonance compound, with higher density of resonant protons or with peak resonances farther from that of water (which could be achieved with lanthanide chelates, for example (31)).

Compared to FatNav-based motion tracking, the trackDOTS approach can be seen as pursuing a further tradeoff of SNR for increased acquisition speed. Despite their high tolerance to undersampling, FatNavs will typically require at least a few hundred milliseconds to acquire a single volume, with corresponding losses in accuracy as their resolution is decreased and/or acceleration factor increased (23). The tests conducted in this work with accelerated FatNavs suggest that, at acquisition times below 70 ms, DotNavs tend to outperform FatNavs in motion estimation accuracy (Fig. 8). Furthermore, the DotNav TA of 45 ms could be further reduced to approximately 18 ms when acquiring a single echo per readout – or even further if the three projections are obtained with the same excitation (removing two long frequency selective pulses and crushers). This would yield even more favorable tradeoffs between accuracy and speed. The development of fast navigators is highly relevant for host sequences that do not contain regular "dead time" periods (such as to allow T_1 relaxation, or due to SAR constraints, for example), in which a navigator could be inserted without altering the total scan time. GRE-based sequences used for SWI, QSM, time-of-flight imaging, are examples of protocols without significant dead time, and for which the total scan time will thereby increase with the number and duration of any

included navigators. Faster navigators can also be more flexibly inserted within certain host sequences, such as in-between the INV_1 and INV_2 blocks of the MP2RAGE, and even within the blocks, greatly improving the temporal resolution of motion estimates. Furthermore, although in this work the trackDOTS approach was only tested in 3D imaging (where retrospective reconstruction is more straightforward), this technique is also likely be less sensitive to saturation effects imposed by the host sequence than other imaging-based navigators (given the short T_1 of the markers and the fact that motion estimation depends only on the projection peak positions, not their relative signal intensities), allowing it to be integrated in multi-slice 2D imaging sequences and even spectroscopic imaging.

TrackDOTS-based field correction

In contrast with motion correction, the use of trackDOTS phase information for correction of field perturbations yielded mixed results in image quality. Overall, the estimated offset and 1st order field terms were generally superior, though of similar order of magnitude, to estimates reported in previous studies (6). Oscillations coupled to the respiratory cycle could be robustly observed for all subjects during deep breathing (Fig. 9), and in those subjects that performed the task without large associated head motion, field correction resulted in clear improvements for the GRE images (Fig. 10). On the other hand, in subjects with larger motion, the correction was considerably less effective. The most likely cause for this disparity is an interaction between head motion and field estimation at the markers, arising due to the perturbations in B_0 homogeneity created by the head itself, within and around its volume (29). Due to susceptibility differences between the head tissues and surrounding air, the head creates a dipole-shaped perturbation in B_0, with concomitant shifts in resonance frequency that can reach up to 1000 Hz at 7 T (Supporting Fig. S3). When the head rotates in B_0, the markers are displaced with it, but the field distribution does not rotate together with the object (except when the rotation axis is parallel to B_0). As a result, the local field affecting each marker, and thereby its resonant frequency, will change with head orientation. This could pose an important bias for motion estimation, given that the projection readout is frequency-encoded, but was rendered negligible (for reasonable ranges of head rotation) by the fairly high bandwidth used (781 Hz/Px). However, for the purpose of field monitoring, where the fluctuations of interest are in a range of only tens of Hz, this effect can add a significant confound to the estimates. Consistent with this hypothesis, in tests performed with

concurrent DotNav and double-echo GRE acquisitions (the latter serving as reference, or gold standard), DotNav-based field estimates showed consistently higher correlation with the motion parameters than GRE-based estimates, and their deviation tended to be larger when the correlation with motion was higher as well, suggesting a reduced accuracy of DotNavs in such cases. Also important, this dependence tended to be particularly accentuated for the G_y term (Fig. 9, right), which could explain the ineffectiveness of first-order field correction on the T_2^*-weighted GRE acquisitions.

In the T_2^*-weighted acquisitions, in subjects with larger motion, the timecourses of field estimates were also strongly correlated to those of motion, and regressing out the motion timecourses significantly improved the field correction step in image reconstruction (Supporting Fig. S1 B). This regression step was intended to provide a 1st order correction to the motion-induced field perturbations around the head, given that the field is expected to change linearly with small head rotations (29). It is, however, a suboptimal solution because "true" field perturbations, such as due to breathing, are also correlated with head motion (32), and can then be partially regressed out as well, compromising sensitivity. In agreement with this, the motion-regressed field corrections were roughly of similar quality to reconstructions without correction, although superior to non-regressed corrections (Supporting Fig. S1 B). It is thus likely that an additional monitoring source would be needed to disentangle these coupled contributions.

Overall, the 1st order field terms were found particularly challenging to measure accurately. The SNR of these terms is limited by the spacing between markers around the head, as well as the terms that limit the field estimation at each marker, namely the TE difference and the SNR of the marker at either echo. The marker positions were chosen to preserve subject comfort while trying to maximize spatial coverage. Additionally, no markers were positioned at the very top of the head, as this region exhibits the strongest susceptibility-related field shifts (Supporting Fig. S3), which actually prevented markers tested in that location to be excited with the current frequency-selective pulse. Finding alternative off-resonance markers with larger frequency shifts relative to water (3 kHz, for example) would help avoiding this problem. Additionally, an increase in the TE difference could increase the measurement SNR concomitantly, provided that the T_2^* can be made adequately long. Future work could thereby explore the use of less heavily-doped marker solutions, which could allow an alternative DotNav design consisting of a single excitation followed by two readout blocks, each consisting of the three projections, for field estimation.

This could yield a time-efficient option for improving both the SNR of position estimates (a 90° pulse could be used for excitation, for instance) and that of field estimates (increased TE difference, to accommodate the two orthogonal projections in between the field readouts).

Real-time motion and field monitoring

With some methodological changes, the trackDOTS approach could potentially be adapted for real-time motion and B_0 field monitoring. The non-linear optimization method currently used to isolate marker projections can be parallelized (since each marker combination is determined independently), or simply replaced by a less-effective, but faster nearest-coil selection method. The robust least-squares estimation approach can be replaced by a simpler weighted least-squares step, with weights based on the initial peak quality values, for example. In this manner, motion and field estimates could be obtained in under 50 ms per timepoint (using Matlab on an Intel Core i7-2600 CPU at 3.40 GHz). On the other hand, the proposed changes are likely to bring compromises in accuracy and robustness that would need to be carefully assessed, given that real-time correction approaches are required to be highly robust. In this regard, the use of real-time adaptive estimation methods (adapting the projection weights based on the errors of previous iterations, for example), and the use of higher-SNR/higher-chemical shift markers, as discussed above, could prove valuable to counter these potential losses.

Conclusions

This work demonstrates that motion tracking and correction can be performed using a discrete set of off-resonance markers monitored with fast MR navigators. The approach can measure even sub-millimeter involuntary head motion, and offers clear improvements in image quality at 7 T, particularly valuable for high-spatial resolution imaging. When used for B_0 field monitoring, trackDOTS navigators can robustly detect deep breathing-induced oscillations. Coupling between head motion and field fluctuations can prevent an accurate field estimation; in cases of moderate motion, however, field estimation and correction can be quite effective, with clear improvements in T_2^*-weighted image quality.

Acknowledgments

This work was supported by Centre d'Imagerie BioMédicale (CIBM) of the UNIL, UNIGE, HUG, CHUV, EPFL and the Leenaards and Jeantet Foundations, as well as the Swiss National Foundation through Grants 132821 and 205321–153564.

Figures

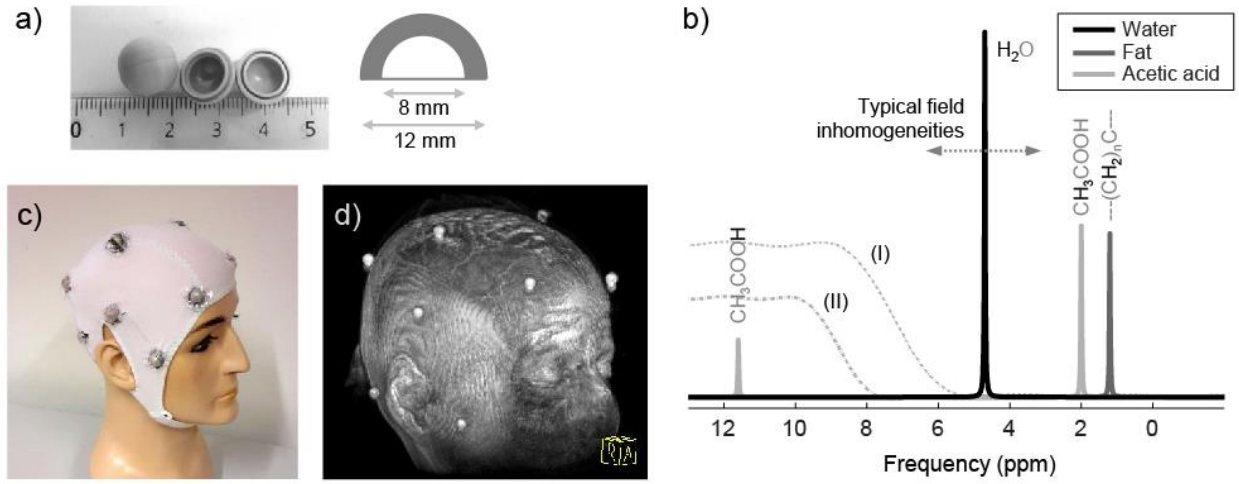

Fig. 1. TrackDOTS implementation. a) Spherical PEEK enclosing for each marker. b) Simulated proton MR spectrum with the water and main fat resonance peaks, together with the two resonance peaks of acetic acid (CH_3COOH) – the acid group peak (11.6 ppm) was targeted in this work as off-resonance marker; the peak amplitudes are set according to their relative intensity when in pure solution; the expected range of typical field inhomogeneities at 7 T (~1 kHz) is represented with a dotted arrow, and the two dashed curves show the excitation profiles of a 2 ms (I) and 3 ms (II) sinc pulse with a time-bandwidth product of 2.7. c) Full set of markers attached to head cap. d) Surface rendering of a human head and the marker signals from a water GRE image – each marker shows two "ghosts" in the Z-direction (readout direction) corresponding to the two distinct resonance peaks of acetic acid.

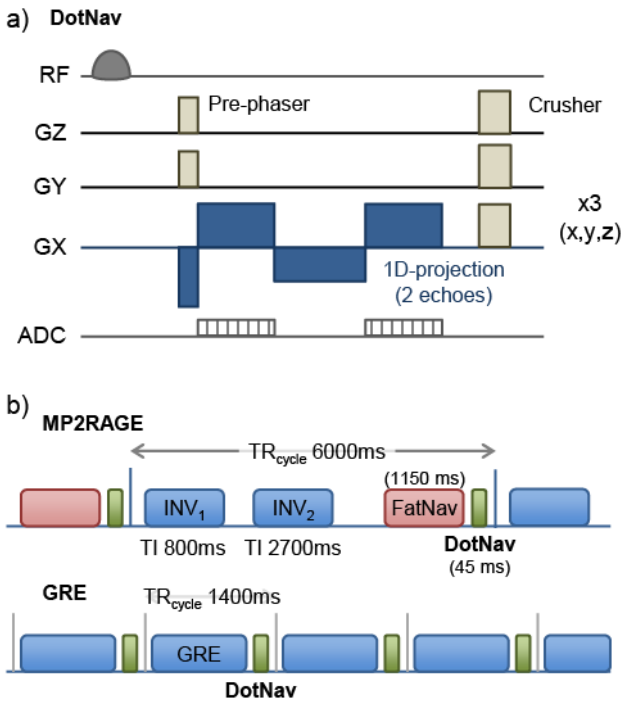

Fig. 2. Pulse sequence diagrams for (a) the DotNav module and (b) the two anatomical sequences investigated in this work: (upper) a 3D MP2RAGE sequence with integrated FatNavs and DotNavs, placed in between the second GRE k-space plane acquisition (INV_2) and the following inversion pulse, and (lower) a 3D GRE sequence with integrated DotNavs, placed in between each k-space plane acquisition. Diagrams are not drawn to scale.

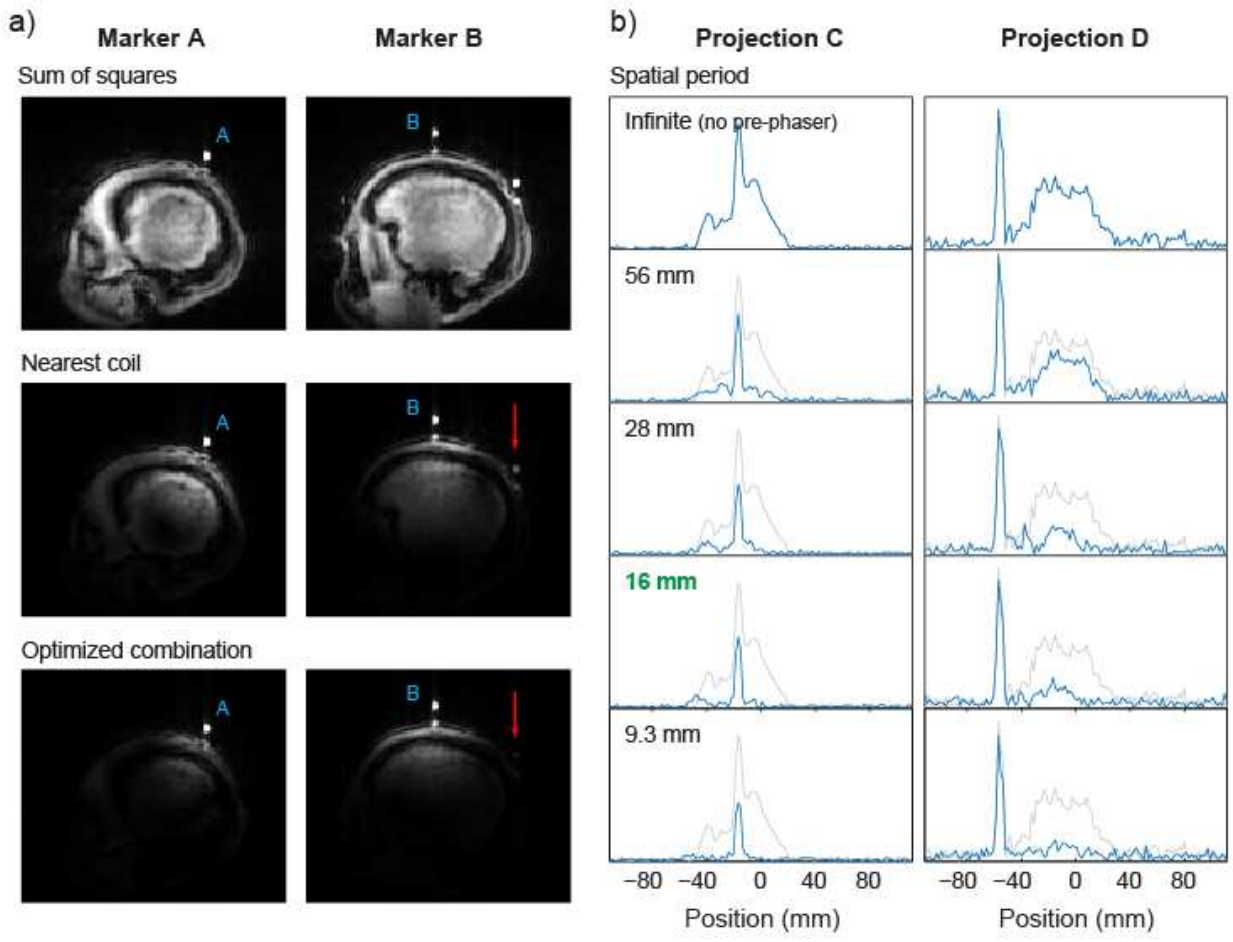

Fig. 3. Marker discrimination from the remaining markers and signal contaminations. a) Different coil combination approaches and the resulting sensitivity for two example markers; the red arrow indicates the presence of a second marker in the FOV, which is differently attenuated by each of the combination approaches. b) The impact of adding pre-phaser gradients to the DotNav on two example marker projections, for different levels of imposed spatial phase periodicity; the grey curve shows the non-phased projection, for reference; pre-phasers imposing a 16 mm periodicity (equal to twice the marker diameter, shown in green) were used in this work. The labels A–D are arbitrary; the corresponding markers and projections were chosen as to illustrate the main effects achieved with these techniques.

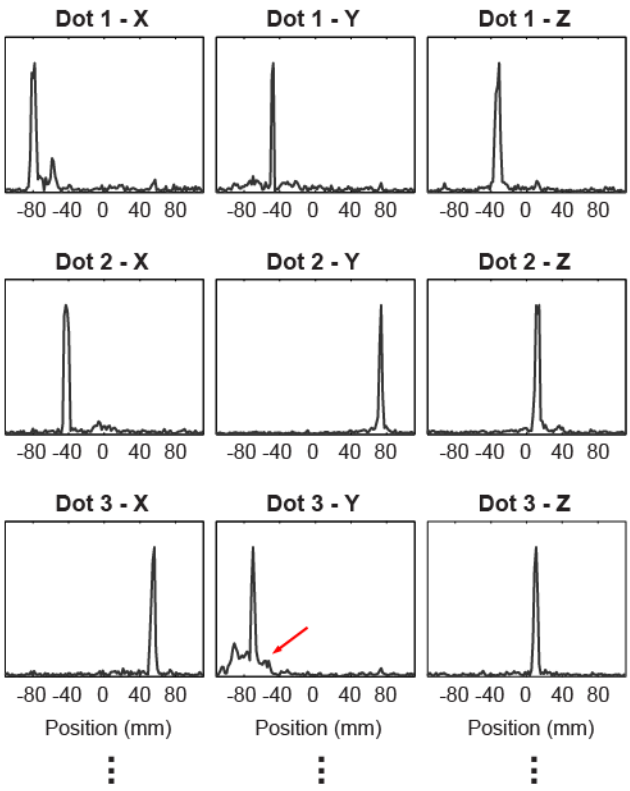

Fig. 4. Examples of DotNav marker projections after marker-specific coil combination. The vertical scaling is adjusted to the peak amplitude in each plot. The red arrow indicates a lower-quality projection where background signal contaminations overlap with the projection peak; the contribution from this estimate is likely to be down-weighted in the robust least-squares approach for motion estimation.

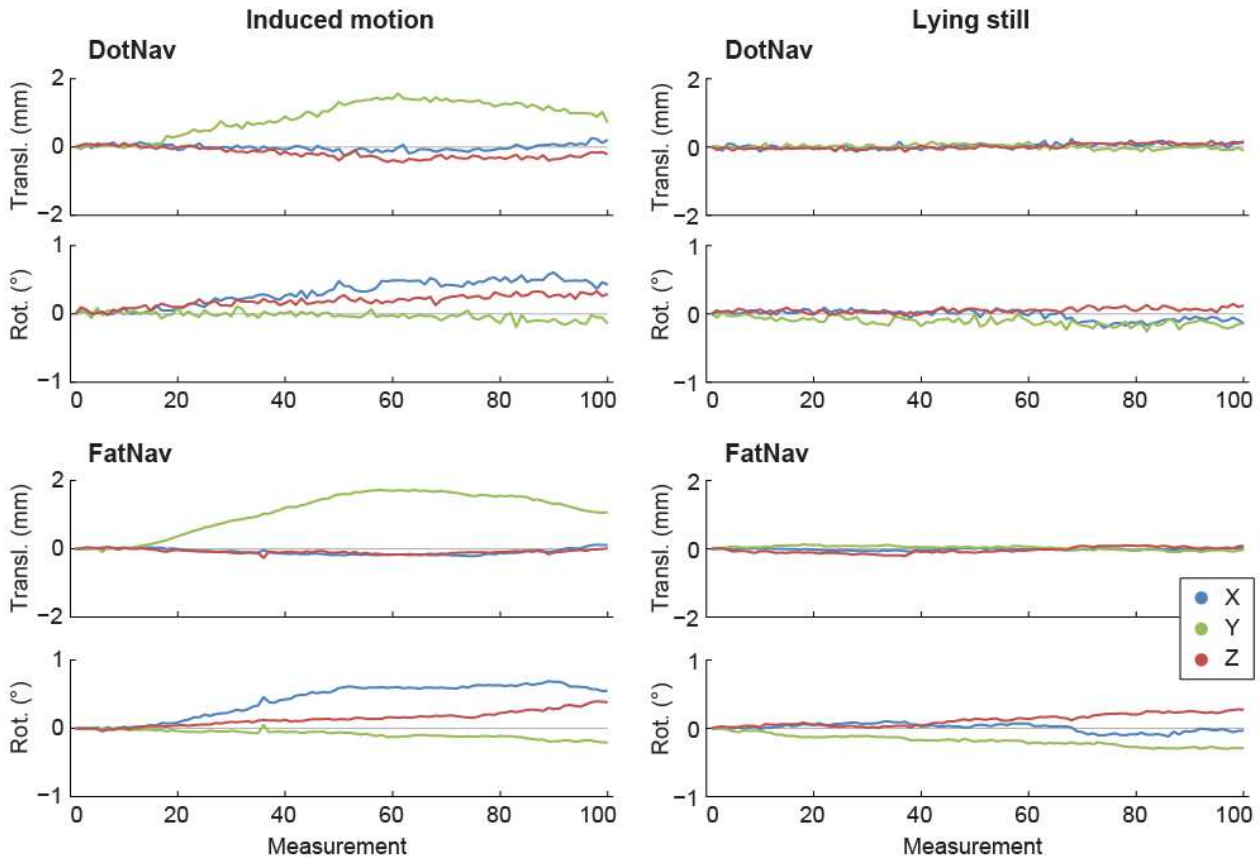

Fig. 5. Typical head translation and rotation timecourses found during the MP2RAGE acquisition with and without externally-induced motion, as estimated by either DotNavs or FatNavs.

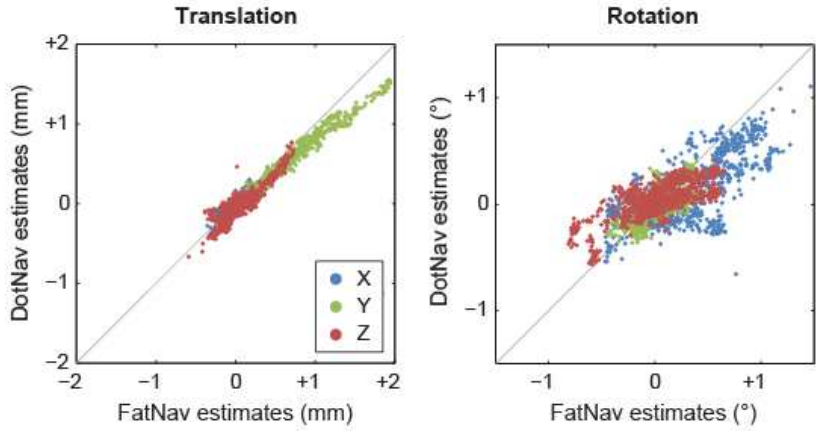

Fig. 6. Comparison between DotNav and FatNav estimates for head translation and rotation. The plots contain data from all subjects and both MP2RAGE runs (with and without induced motion) pooled together.

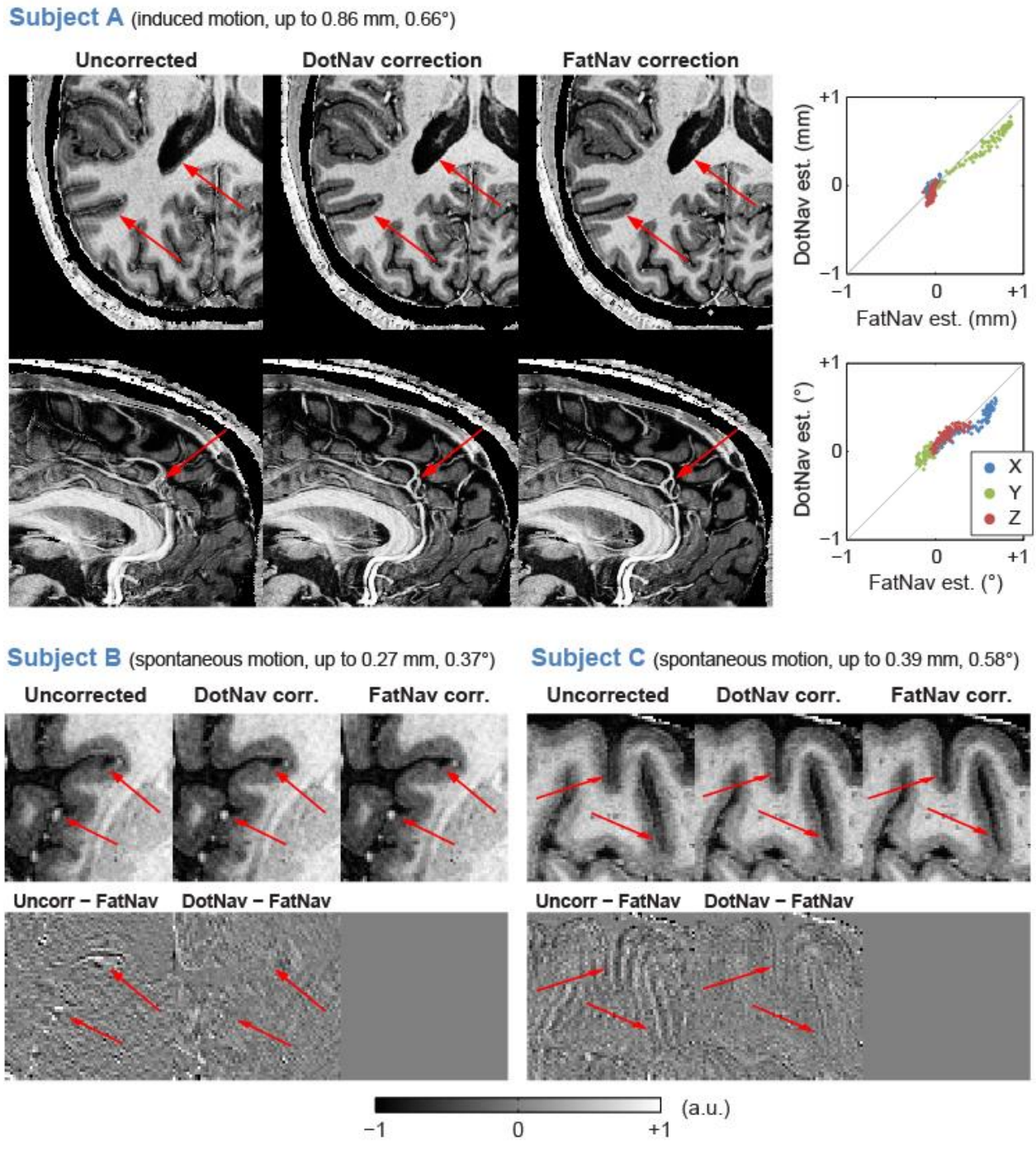

Fig. 7. The impact of retrospective motion correction for three example subjects with (A) and without (B, C) externally-induced motion; the maximum range of head translation and rotation during each acquisition is indicated in the title. Motion correction was performed using either DotNav or FatNav estimates; the red arrows highlight anatomical features clearly improved after correction. For the spontaneous motion examples, difference images between uncorrected or DotNav-corrected reconstructions, relative to FatNav-corrected reconstructions, are also presented to more clearly illustrative these improvements.

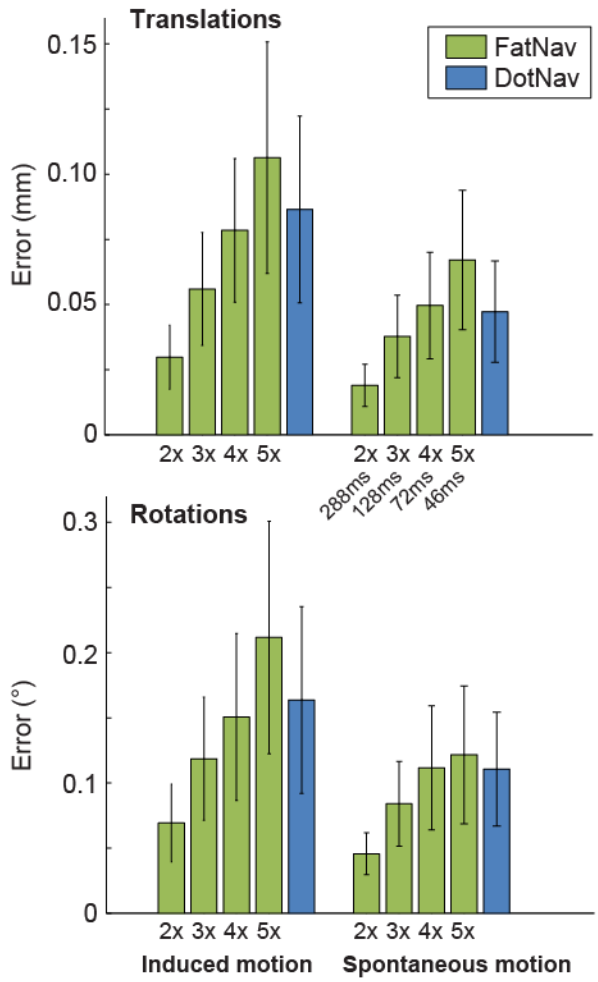

Fig. 8. Average absolute error of motion estimates obtained with DotNavs and with FatNavs at increasing level of acceleration, relative to reference estimates from the originally-acquired FatNavs. The 2 / 3 / 4 / 5× accelerated versions were obtained post-acquisition by systematically

cropping the k-space of the original FatNavs, and correspond to acquisition times of 288 / 128 / 72 / 46 ms, respectively.

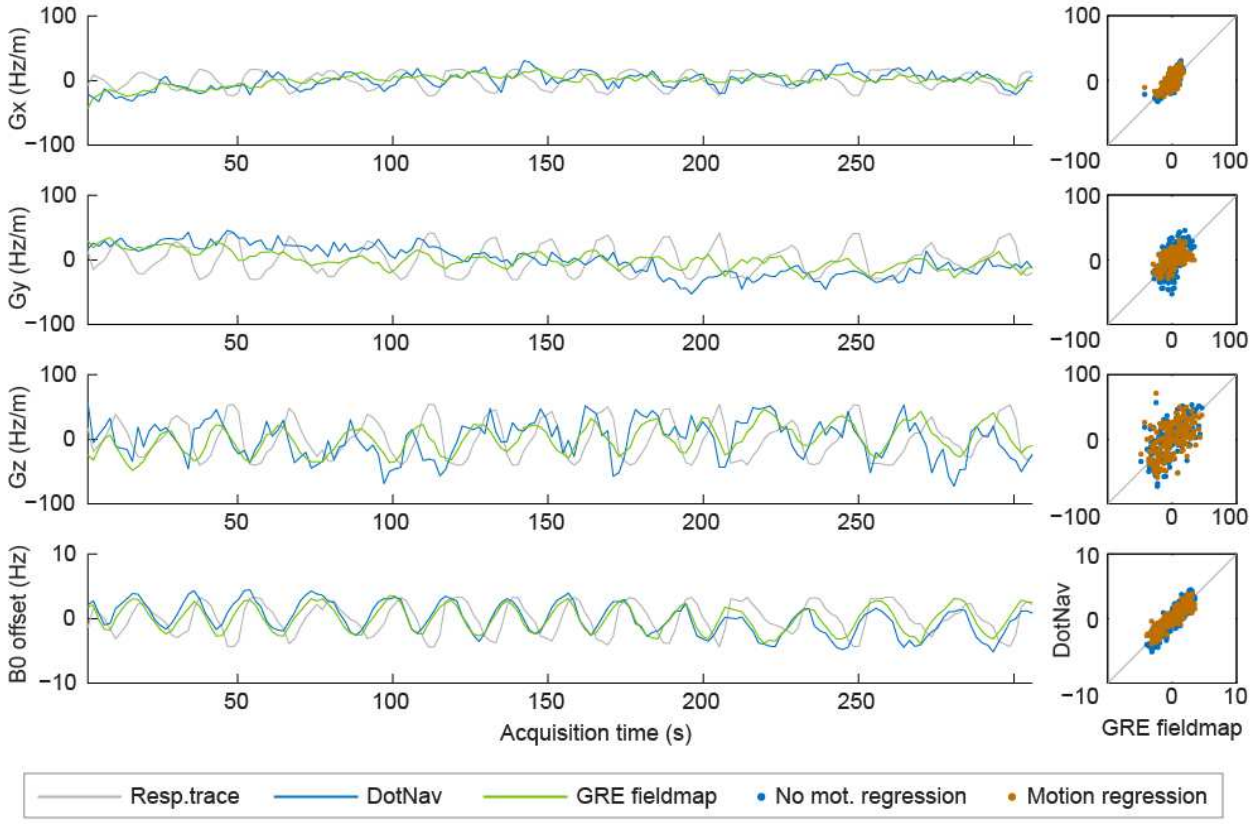

Fig. 9. Left: TrackDOTS-based B_0 field monitoring during slow, deep breathing, for an example subject, without regressing out head motion. Concurrent field estimates obtained with a fast double-echo GRE acquisition (TA = 1.8 s) are shown in green for comparison. The subject's respiratory trace, as measured by a pneumatic belt, is also included in grey for reference. Right: comparison between the DotNav and GRE fieldmap estimates, before and after motion regression.

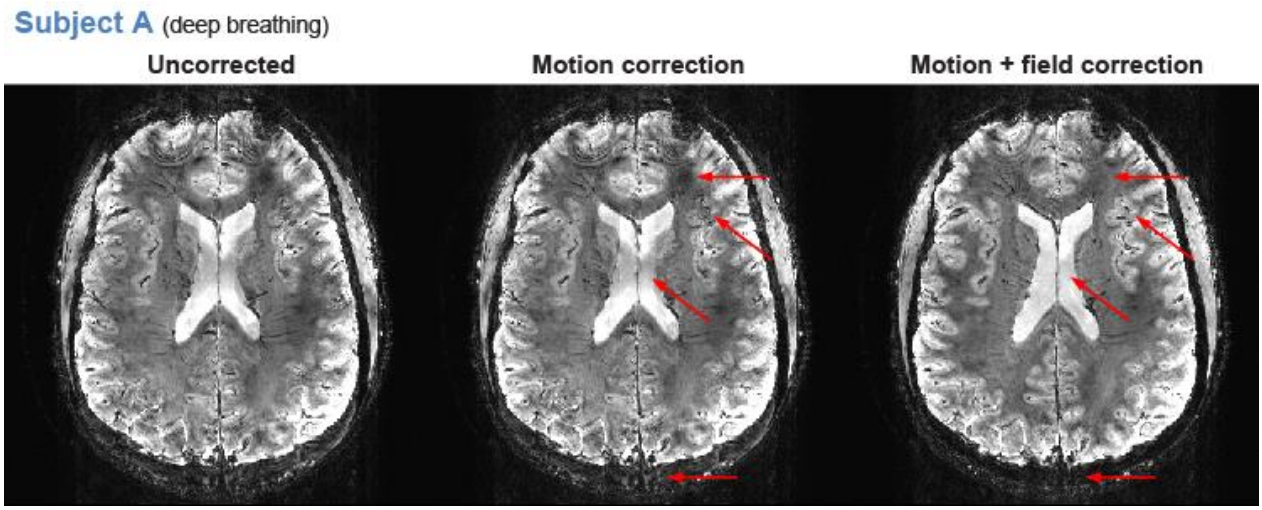

Fig. 10. The impact of correcting for fluctuations in B_0 during a long-TE GRE acquisition with deep breathing, for an example subject. The red arrows highlight clear improvements obtained with field correction, including ghosting reduction, increases in grey-matter to white-matter contrast, and mitigation of local signal drops.

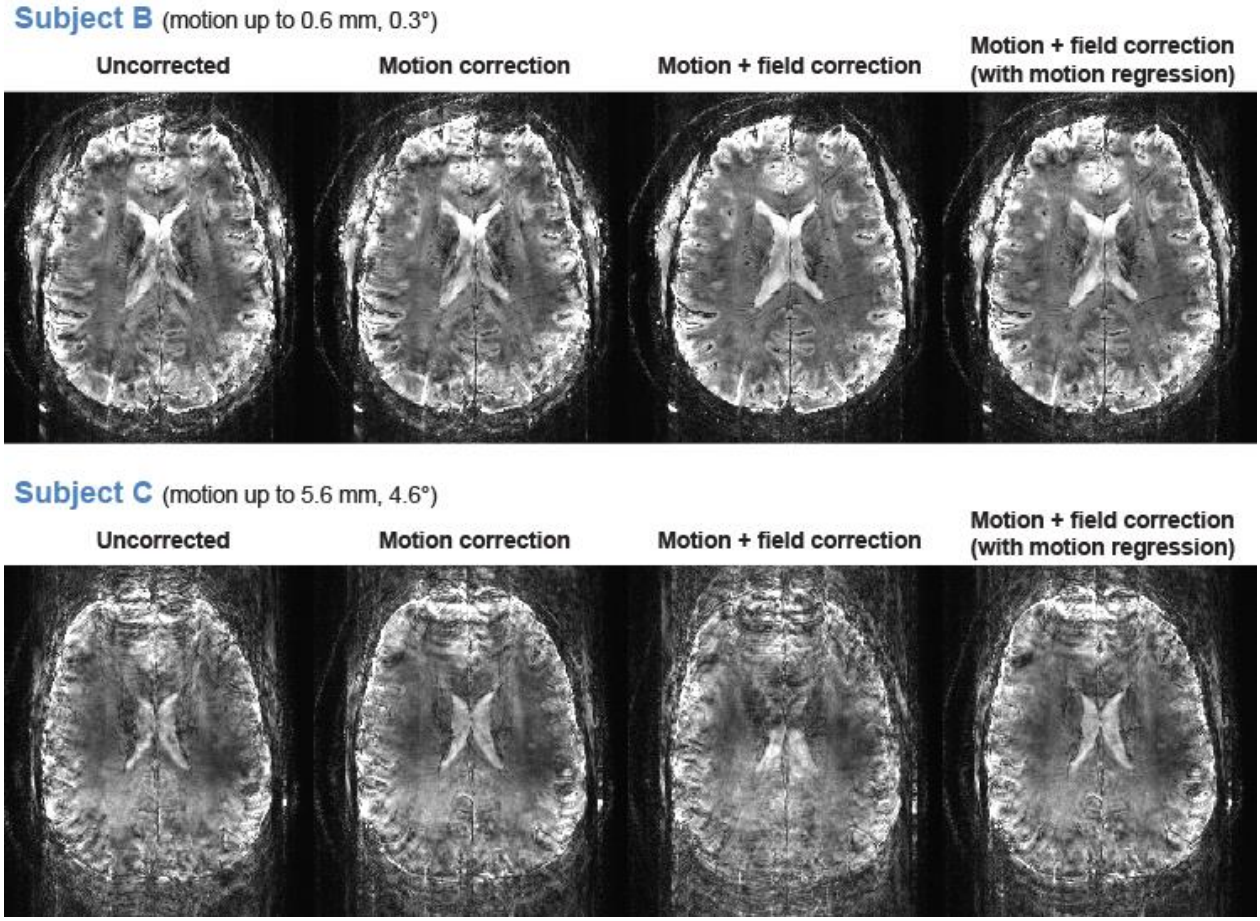

Supporting Fig. S1. The impact of correcting for fluctuations in B_0 during a long-TE GRE acquisition with deep breathing, for two example subjects with moderate (A) and accentuated head motion (B).

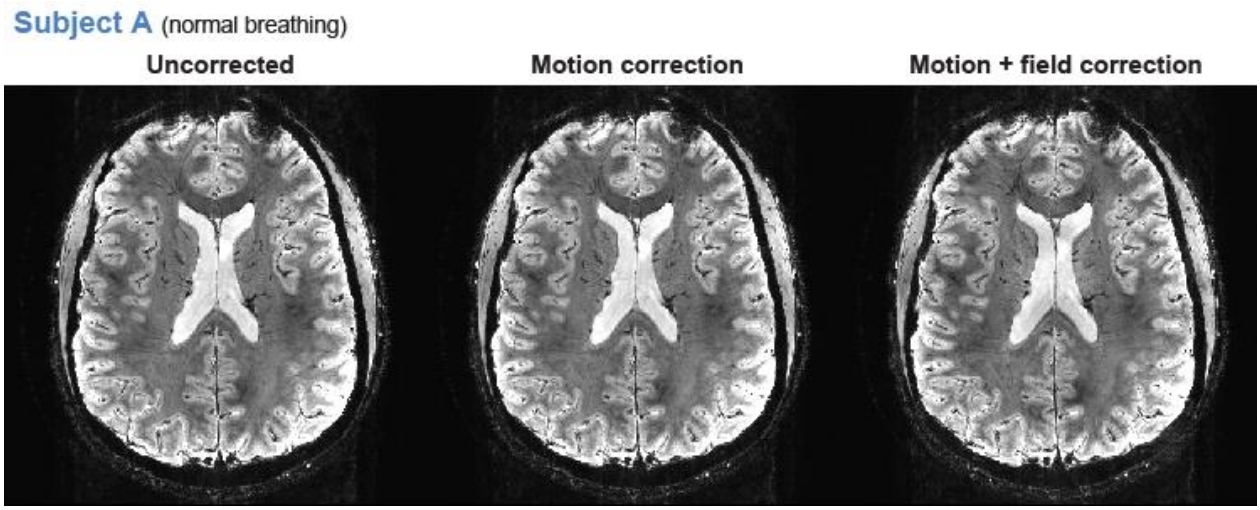

Supporting Fig. S2. Correction of B_0 fluctuations during a long-TE GRE acquisition with normal breathing, for an example subject.

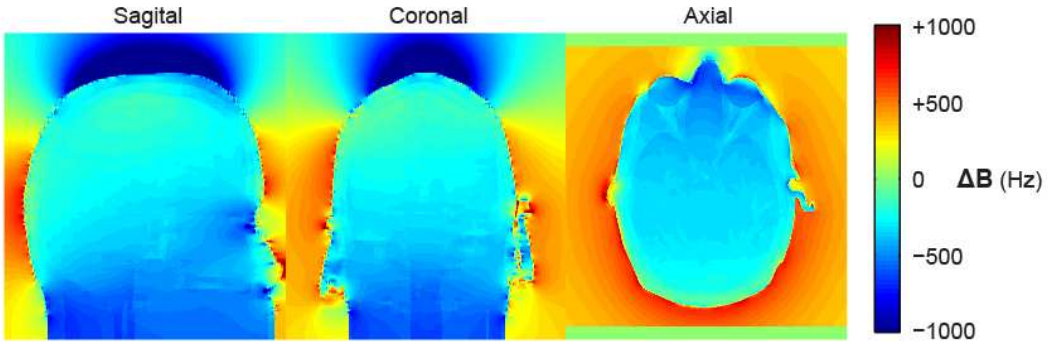

Supporting Fig. S3. Simulated map of susceptibility-induced magnetic field deviations inside and outside the head, at 7 T, based on a realistic model of susceptibility distribution in a human head.

References

1. Reuter M, Tisdall MD, Qureshi A, Buckner RL, van der Kouwe AJ, Fischl B. Head motion during MRI acquisition reduces gray matter volume and thickness estimates. NeuroImage 2015;107:107-115.

2. Maclaren J, Armstrong BS, Barrows RT, Danishad KA, Ernst T, Foster CL, Gumus K, Herbst M, Kadashevich IY, Kusik TP, Li Q, Lovell-Smith C, Prieto T, Schulze P, Speck O, Stucht D, Zaitsev M.

Measurement and correction of microscopic head motion during magnetic resonance imaging of the brain. PloS one 2012;7(11):e48088.

3. van Gelderen P, de Zwart JA, Starewicz P, Hinks RS, Duyn JH. Real-time shimming to compensate for respiration-induced B0 fluctuations. Magnetic resonance in medicine 2007;57(2):362-368.

4. Haacke EM, Xu Y, Cheng YC, Reichenbach JR. Susceptibility weighted imaging (SWI). Magnetic resonance in medicine 2004;52(3):612-618.

5. Shmueli K, de Zwart JA, van Gelderen P, Li TQ, Dodd SJ, Duyn JH. Magnetic susceptibility mapping of brain tissue in vivo using MRI phase data. Magnetic resonance in medicine 2009;62(6):1510-1522.

6. Duerst Y, Wilm BJ, Wyss M, Dietrich BE, Gross S, Schmid T, Brunner DO, Pruessmann KP. Utility of real-time field control in T2 *-Weighted head MRI at 7T. Magnetic resonance in medicine 2016;76(2):430-439.

7. Versluis MJ, Sutton BP, de Bruin PW, Bornert P, Webb AG, van Osch MJ. Retrospective image correction in the presence of nonlinear temporal magnetic field changes using multichannel navigator echoes. Magnetic resonance in medicine 2012;68(6):1836-1845.

8. Wen J, Cross AH, Yablonskiy DA. On the role of physiological fluctuations in quantitative gradient echo MRI: implications for GEPCI, QSM, and SWI. Magnetic resonance in medicine 2015;73(1):195-203.

9. Federau C, Gallichan D. Motion-Correction Enabled Ultra-High Resolution In-Vivo 7T-MRI of the Brain. PloS one 2016;11(5):e0154974.

10. Zaitsev M, Dold C, Sakas G, Hennig J, Speck O. Magnetic resonance imaging of freely moving objects: prospective real-time motion correction using an external optical motion tracking system. NeuroImage 2006;31(3):1038-1050.

11. Schulz J, Siegert T, Reimer E, Labadie C, Maclaren J, Herbst M, Zaitsev M, Turner R. An embedded optical tracking system for motion-corrected magnetic resonance imaging at 7T. MAGMA 2012;25(6):443-453.

12. Forman C, Aksoy M, Hornegger J, Bammer R. Self-encoded marker for optical prospective head motion correction in MRI. Medical image analysis 2011;15(5):708-719.

13. van der Kouwe AJ, Benner T, Dale AM. Real-time rigid body motion correction and shimming using cloverleaf navigators. Magnetic resonance in medicine 2006;56(5):1019-1032.

14. Tisdall MD, Hess AT, Reuter M, Meintjes EM, Fischl B, van der Kouwe AJ. Volumetric navigators for prospective motion correction and selective reacquisition in neuroanatomical MRI. Magnetic resonance in medicine 2012;68(2):389-399.

15. White N, Roddey C, Shankaranarayanan A, Han E, Rettmann D, Santos J, Kuperman J, Dale A. PROMO: Real-time prospective motion correction in MRI using image-based tracking. Magnetic resonance in medicine 2010;63(1):91-105.

16. Kober T, Marques JP, Gruetter R, Krueger G. Head motion detection using FID navigators. Magnetic resonance in medicine 2011;66(1):135-143.

17. Babayeva M, Kober T, Knowles B, Herbst M, Meuli R, Zaitsev M, Krueger G. Accuracy and Precision of Head Motion Information in Multi-Channel Free Induction Decay Navigators for Magnetic Resonance Imaging. IEEE transactions on medical imaging 2015;34(9):1879-1889.

18. Ooi MB, Krueger S, Thomas WJ, Swaminathan SV, Brown TR. Prospective real-time correction for arbitrary head motion using active markers. Magnetic resonance in medicine 2009;62(4):943-954.

19. Haeberlin M, Kasper L, Barmet C, Brunner DO, Dietrich BE, Gross S, Wilm BJ, Kozerke S, Pruessmann KP. Real-time motion correction using gradient tones and head-mounted NMR field probes. Magnetic resonance in medicine 2015;74(3):647-660.

20. Gallichan D, Marques JP, Gruetter R. Retrospective correction of involuntary microscopic head movement using highly accelerated fat image navigators (3D FatNavs) at 7T. Magnetic resonance in medicine 2016;75(3):1030-1039.

21. Barmet C, De Zanche N, Wilm BJ, Pruessmann KP. A transmit/receive system for magnetic field monitoring of in vivo MRI. Magnetic resonance in medicine 2009;62(1):269-276.

22. Engstrom M, Martensson M, Avventi E, Norbeck O, Skare S. Collapsed fat navigators for brain 3D rigid body motion. Magnetic resonance imaging 2015;33(8):984-991.

23. Gallichan D, Marques JP. Optimizing the acceleration and resolution of three-dimensional fat image navigators for high-resolution motion correction at 7T. Magnetic resonance in medicine 2016.

24. Ooi MB, Aksoy M, Maclaren J, Watkins RD, Bammer R. Prospective motion correction using inductively coupled wireless RF coils. Magnetic resonance in medicine 2013;70(3):639-647.

25. Marques JP, Kober T, Krueger G, van der Zwaag W, Van de Moortele PF, Gruetter R. MP2RAGE, a self bias-field corrected sequence for improved segmentation and T1-mapping at high field. NeuroImage 2010;49(2):1271-1281.

26. Deistung A, Rauscher A, Sedlacik J, Stadler J, Witoszynskyj S, Reichenbach JR. Susceptibility weighted imaging at ultra high magnetic field strengths: theoretical considerations and experimental results. Magnetic resonance in medicine 2008;60(5):1155-1168.

27. Fessler JA, Sutton BP. Nonuniform fast Fourier transforms using min-max interpolation. Ieee T Signal Proces 2003;51(2):560-574.

28. Gretsch F, Kober T, Gallichan D, Waszak M, Marques JP, Gallichan D. High Temporal Resolution Retrospective Motion and B0 Correction Using FIDNavs and Segmented FatNavs at 7T. Proceedings of the 24th Annual Meeting of ISMRM; 2016; Singapore. (Proceedings of the 24th Annual Meeting of ISMRM).

29. Marques JP, Bowtell R. Application of a fourier-based method for rapid calculation of field inhomogeneity due to spatial variation of magnetic susceptibility. Concept Magn Reson B 2005;25B(1):65-78.

30. Sengupta S, Tadanki S, Gore JC, Welch EB. Prospective real-time head motion correction using inductively coupled wireless NMR probes. Magnetic resonance in medicine 2014;72(4):971-985.

31. Viswanathan S, Kovacs Z, Green KN, Ratnakar SJ, Sherry AD. Alternatives to gadolinium-based metal chelates for magnetic resonance imaging. Chemical reviews 2010;110(5):2960-3018.

32. Andersen M, Hanson LG, Madsen KH, Wezel J, Boer V, van der Velden T, van Osch MJ, Klomp D, Webb AG, Versluis MJ. Measuring motion-induced B0 -fluctuations in the brain using field probes. Magnetic resonance in medicine 2016;75(5):2020-2030.